International Journal of Heat and Mass Transfer 55 (2012) 7561–7569

Contents lists available at SciVerse ScienceDirect

International Journal of Heat and Mass Transfer

journal homepage: www.elsevier.com/locate/ijhmt

Numerical modeling and experimental validation of heat transfer and flow resistance on the shell side of a shell-and-tube heat exchanger with flower baffles

Yonghua You, Aiwu Fan *, Suyi Huang, Wei Liu

School of Energy and Power Engineering, Huazhong University of Science and Technology, Wuhan 430074, China

ARTICLE INFO

Article history:
Received 17 May 2012
Received in revised form 20 July 2012
Accepted 20 July 2012
Available online 19 August 2012

Keywords:
Shell-and-tube heat exchanger
Flower baffle
Numerical modeling
Experimental validation
Thermal augmentation
Flow resistance

ABSTRACT

CFD simulation has become a powerful and popular tool for the thermal hydraulic design and analysis of heat exchangers. However, the computation load is usually too heavy to simulate a whole shell-and-tube heat exchanger (STHX) applying the traditional modeling method. In the present study, a numerical model based on the concepts of porosity and permeability is developed to obtain the shell-side thermal hydraulic performances. In this model, the distributed resistances and heat sources, as well as the distributed turbulence kinetic energy and its dissipation rate are introduced to account for the impacts of tubes on the fluid. The numerical model is solved over Re = 6813–22,326 for the shell side of a STHX with flower baffles, and reasonable accuracy is demonstrated by the comparison with test data (maximum relative deviation within 15%). With this model, the velocity and temperature fields, together with the distribution of convective heat transfer coefficient, are obtained and presented to help analyzing the underlying mechanism of shell-side thermal augmentation. The present work shows that this model is economic and effective in the thermal hydraulic design and analysis of a whole device.

1. Introduction

Shell-and-tube heat exchangers (STHXs) are widely applied in various industrial fields such as petroleum refining, power generation and chemical process, etc. Tremendous efforts have been made to improve the performances on the tube side [1–5]. For the shell side, the velocity and temperature fields are relatively complicated and the thermal hydraulic performance depends on the baffle elements to a great extent. In the traditional shell-and-tube heat exchangers with segmental baffles (SG-STHXs), round plates with cut are always used for the support of tubes [6–10]. Those baffles can also intensify the fluid flow which leads to heat transfer enhancement on the shell side. However, the flow resistance and harmful vibration level are large. Besides, the large-scale "dead" flow regions at the corners decrease the effective heat transfer area and facilitate the fouling on tubes. To solve these problems, various new types of baffles have been developed [11]. To give some examples, orifice baffles were designed to reduce the "dead" flow region and for heat transfer enhancement [12]. Rod baffles was originally developed to decrease the vibration level, which also showed good thermal hydraulic performances [13,14]. Helical baffles were proposed as the support of tubes and demonstrated good thermal hydraulic performance, low vibration level and less fouling as well [15,16]. In addition, ring support [17] and twisted self-supported tube [11] were also proposed and investigated.

Experimental test is a common method to investigate the thermal hydraulic performance on the shell side of heat-exchangers. However, experiments are relatively expensive and time-consuming. In addition, flow visualization on the shell side is also hard to deal with. Nowadays, the numerical method has become an economic alternative for the researches of STHXs, through which the detailed flow pattern and temperature field could be obtained with much less difficulties. Nevertheless, the computation load is always too heavy to model the whole device for desired information with reasonable accuracy. For this reason, a simplified model based on volumetric porosity and surface permeability was proposed and developed to model the shell-side flow and heat transfer [18–25]. With this method, the computation load decreases substantially while remaining a relatively high accuracy.

As mentioned above, STHXs with helical baffles have demonstrated a good overall performance on the shell side [26–28]. However, continuous helical baffles are difficult to manufacture, which hinders their wide applications. In order to induce spiral flow on the shell side while facilitate the manufacture, the STHX with flower baffles (FB-STHX) was designed in our group [29], in which round plates with two quadrants hollow were installed alternately in the shell as the support for tubes. And experimental investigations showed that this heat exchanger had a good thermal hydraulic

* Corresponding author. Address: School of Energy and Power Engineering, Huazhong University of Science and Technology, 1037 Luoyu Road, Wuhan 430074, China. Tel.: +86 27 87542618; fax: +86 27 87540724.
E-mail addresses: faw@mail.hust.edu.cn, catia315@163.com (A. Fan).

0017-9310/$ - see front matter © 2012 Elsevier Ltd. All rights reserved.
http://dx.doi.org/10.1016/j.ijheatmasstransfer.2012.07.058

Nomenclature

A	heat transfer area, m^2
c_p	specific heat of constant pressure, J/(kg K)
d_i	inner diameter of tubes, m
d_o	outer diameter of tubes, m
D	inner diameter of shell, m
d_e	shell-side characteristic dimension, m
f	friction factor
f_S	surface permeability
f_V	volumetric porosity
h	convective heat transfer coefficient, W/(m^2 K)
k	coefficient, W/(m^2 K)
K	overall heat transfer coefficient, W/(m^2 K)
L	tube length, m
n	tube number
m	mass flow rate, kg/s
p	static pressure, Pa
Δp	static pressure loss, Pa
Pr	Prandtl number
Q	heat flux, W
Re	Reynolds number
t	time, s
T	static temperature, K
ΔT	temperature difference, K
u	velocity, m/s
x	coordinate axis, m
ρ	density, kg/m^3
μ	dynamic viscosity, N s/m^2
ε	turbulent kinetic energy dissipation rate, m^2/s^3
λ	thermal conductivity, W/(m K)
α	geometry angle of baffle, °
Ω	specific surface area, m^2/m^3

Subscripts

ex	exit
i, j	tensor
in	inlet
l	laminar
m	the mean value
s	shell-side
t	tube-side; turbulent

performance. In the present study, we are to develop a numerical model based on the concepts of porosity and permeability to obtain shell-side thermal hydraulic performances for the FB-STHX, and detailed flow and temperature fields will also be shown to help analyzing the underlying mechanisms. The numerical model will be validated with experimental data presented in [29,30].

2. Numerical model

A FB-STHX is of large dimension and complicated structure, thus the computation load is too large to obtain the flow and temperature fields on the shell side with traditional CFD modeling method, where the details of tube bundles need to be modeled and computed. For the sake of simplification, we borrow the concepts of volumetric porosity and surface permeability from porous media in the present work. The impacts of tubes on heat transfer and fluid flow on the shell side are considered by introducing a distributed heat source and a distributed flow resistance, which are determined by some correlations obtained through experiments. By doing this, the spaces occupied by tubes and the shell-side fluid could be meshed in the same grid system, which leads to substantial reduction in the cell number and computation load.

2.1. Governing equations on the shell side

In the present work, we are to compute the fluid flow and heat transfer on the shell side of the FB-STHX used in our previous experimental investigation [29], with the *Re* number ranging from 6813 to 22,326. The following assumptions were made for the derivation of governing equations:

(1) The working fluid on the shell side is continuous, incompressible, isotropic and Newtonian.
(2) Both the volumetric porosity and surface permeability are uniform in the tube-fluid mixed region; however, the impacts of tubes on fluid are non-uniform in different directions, which are reflected by the distributed resistances and heat source.
(3) The effect of gravity is negligible, and the viscous heating or thermal radiation is ignored.

Based on the above assumptions, the conservation equations of continuity, momentum and energy are presented below in a tensor form in the Cartesian coordinate system [19,20,23].

Continuity equation:

$$\frac{\partial(\rho f_V)}{\partial t}+\frac{\partial(\rho f_S u_j)}{\partial x_j}=0 \tag{1}$$

Momentum equation:

$$\frac{\partial(\rho f_V u_i)}{\partial t}+\frac{\partial(\rho f_S u_i u_j)}{\partial x_j}=-f_S\frac{\partial p_i}{\partial x_i}+\frac{\partial}{\partial x_j}\left(f_S\mu_{eff}\left(\frac{\partial u_i}{\partial x_j}+\frac{\partial u_j}{\partial x_i}\right)\right)-f_i\frac{\rho}{2}|u_i|u_i \tag{2}$$

Energy equation:

$$\frac{\partial(\rho c_p f_V T)}{\partial t}+\frac{\partial(\rho c_p T f_S u_j)}{\partial x_j}=\frac{\partial}{\partial x_j}\left(f_S\lambda_{eff}\left(\frac{\partial T}{\partial x_j}\right)\right)+\Omega K(T_t-T) \tag{3}$$

where all the parameters are for the shell-side fluid, except T_t that stands for the fluid temperature on the tube side. The variable u takes the formulation of physical velocity. The volumetric porosity, f_V, refers to the fraction of the void volume occupied by the fluid in a computation cell, while f_S stands for the surface permeability which equals to the fraction of the open projected flow area. Ω stands for the specific surface area of tube wall in the tube-fluid mixed region.

2.1.1. Distributed resistance on the shell side

The last term on the right hand side in Eq. (2), i.e., $-f_i\frac{\rho}{2}|u_i|u_i$, is the distributed flow resistance which accounts for the influence of tubes on the shell-side fluid flow, and is calculated through some empirical correlations. In this study, Eqs. (4) and (5) are adopted to calculate the cross-flow resistance factor in the staggered and non-staggered tube bundles, respectively [31], where the *Re* number is based on the cross-flow velocity component at the minimum flow area and the outer diameter of tubes acting as the characteristic dimension.

For staggered tube bundles:

$$f_i=4\left[0.23+\frac{0.11}{(\chi_j-1)^{1.08}}\right]\cdot Re_i^{-0.15}\cdot\left(\frac{f_S S_j}{S_j-d_o}\right)^2 \tag{4}$$

For non-staggered (in-line) tube bundles:

$$f_i = 4\left[0.044 + \frac{0.08\chi_i}{(\chi_j - 1)^{0.43+1.13/\chi_i}}\right] \cdot Re_i^{-0.15} \cdot \left(\frac{f_S S_j}{S_j - d_o}\right)^2 \quad (5)$$

where f and f_S are respectively the resistance factor and surface permeability, subscripts i and j stand for the two orthogonal directions normal to the axis of tubes, S refers to the tube pitch, and χ_i is the ratio between tube pitch and outer diameter of tubes, i.e., $\chi_i = S_i/d_o$.

The distributed resistance of axial flow is derived from [19, Eq. (6)], in which subscript x is used for the direction of tube axis, and d_x is the characteristic dimension.

$$f_x = \begin{cases} \frac{31}{Re_x} \cdot \frac{4f_S}{d_x}; & Re_x < 2250 \\ 0.131 Re_x^{-0.294} \cdot \frac{4f_S}{d_x}; & 2250 \leqslant Re_x < 25,000 \\ 0.066 Re_x^{-0.227} \cdot \frac{4f_S}{d_x}; & Re_x \geqslant 25,000 \end{cases} \quad (6)$$

2.1.2. Distributed heat source on the shell side

The distributed heat source, $\beta K(T_t - T)$ in Eq. (3), is used for the heat transfer through tube walls. The parameter K stands for the local overall heat transfer coefficient based on outer wall of tubes. As for a newly built heat exchanger, K is related to the local convective heat transfer coefficients of shell side (h_s) and tube side (h_t), together with the heat conduction resistance of tube wall, as shown in Eq. (7).

$$K = \frac{1}{\frac{1}{h_s} + \frac{d_o}{h_t d_i} + \frac{d_o}{2\lambda_w} \ln\frac{d_o}{d_i}} \quad (7)$$

where λ_w is the heat conductivity of tube walls. For the case where the flow is turbulent and fully developed on the tube side, the value of h_t can be derived from the well-known Dittus–Boelter correlation [32], as shown in Eq. (8).

$$h_t = 0.023 Re_t^{0.8} Pr_t^n \frac{\lambda_t}{d_i}; \quad 10,000 \leqslant Re_t \leqslant 250,000 \quad \& \quad 0.7 \leqslant Pr_t \leqslant 120 \quad (8)$$

where $n = 0.4$ when fluid is heated, otherwise $n = 0.3$.

The heat transfer of the cross flow on the shell side is relatively complicated, which depends on the tube arrangement and cross-flow Re number. In the present study, the empirical correlations of Zukauskas [21,33] are adopted to calculate the local convective heat transfer coefficient of staggered and non-staggered tube bundles on the shell side, as shown in Eqs. (9) and (10), respectively.

For staggered tube bundles:

$$h_s = \begin{cases} 0.71 Re^{0.5} Pr^{0.36} \cdot \frac{\lambda}{d_o}; & 40 < Re < 1000 \\ 0.35 Re^{0.6} Pr^{0.36} \left(\frac{S_t}{S_l}\right)^{0.2} \cdot \frac{\lambda}{d_o}; & 1000 \leqslant Re < 200,000 \quad \& \quad \frac{S_t}{S_l} \leqslant 2.0 \\ 0.4 Re^{0.6} Pr^{0.36} \left(\frac{S_t}{S_l}\right)^{0.2} \cdot \frac{\lambda}{d_o}; & 1000 \leqslant Re < 200,000 \quad \& \quad \frac{S_t}{S_l} > 2.0 \end{cases} \quad (9)$$

For non-staggered (in-line) tube bundles:

$$h_s = \begin{cases} 0.52 Re^{0.4} Pr^{0.36} \cdot \frac{\lambda}{d_o}; & 100 < Re \leqslant 1000 \\ 0.27 Re^{0.63} Pr^{0.36} \cdot \frac{\lambda}{d_o}; & 1000 < Re \leqslant 200,000 \end{cases} \quad (10)$$

where S_t and S_l are respectively the transverse and longitudinal tube distances, while the Re number is based on the cross-flow velocity at the minimum flow area and the outside diameter of tubes.

The effective dynamic viscosity, μ_{eff}, of the momentum equation (Eq. (2)) equals to the sum of the laminar and turbulent dynamic viscosity, i.e., $\mu_{eff} = \mu_l + \mu_t$, and the RNG k–ε turbulence model is adopted for the computation of the turbulent dynamic viscosity. Similar to μ_{eff}, the effective thermal conductivity is the sum of the laminar and turbulent thermal conductivity, i.e., $\lambda_{eff} = \lambda_l + \lambda_t$, and the turbulent one is related to the turbulence viscosity, i.e., $\lambda_t = \mu_t c_p / Pr_t$, where Pr_t is the turbulence Prandtl number. The conservation equations of k and ε are listed below.

For turbulent kinetic energy k:

$$\frac{\partial(\rho f_S k u_j)}{\partial x_j} = \frac{\partial}{\partial x_j}\left(\alpha_k(\mu_t + \mu_l) f_S \frac{\partial k}{\partial x_j}\right) + f_V(G_k - \rho\varepsilon) + G_{t,k} \quad (11)$$

For turbulent kinetic energy dissipation rate ε:

$$\frac{\partial(\rho f_S \varepsilon u_j)}{\partial x_j} = \frac{\partial}{\partial x_j}\left(\alpha_\varepsilon(\mu_t + \mu_l) f_S \frac{\partial \varepsilon}{\partial x_j}\right) + f_V\left(\frac{C_{1\varepsilon}^* \varepsilon}{k} G_k - C_{2\varepsilon}\rho\frac{\varepsilon^2}{k}\right) + G_{t,\varepsilon} \quad (12)$$

where $\mu_t = \rho C_\mu \frac{k^2}{\varepsilon}$; $G_k = 2\mu_t E_{ij} \cdot E_{ij}$; $C_{1\varepsilon}^* = C_{1\varepsilon} - \frac{\eta(1-\eta/\eta_0)}{1+\beta\eta^3}$; $\eta = (2E_{ij} \cdot E_{ij})^{\frac{1}{2}} \frac{k}{\varepsilon}$; $E_{ij} = \frac{1}{2}\left(\frac{\partial u_i}{\partial x_j} + \frac{\partial u_j}{\partial x_i}\right)$. The constants for the RNG k–ε turbulence model are set as below:

$$C_\mu = 0.0845;\ \alpha_k = \alpha_\varepsilon = 1.39;\ C_{1\varepsilon} = 1.42;\ C_{2\varepsilon} = 1.68;\ \eta_0 = 4.377;\ \beta = 0.012.$$

Here, $G_{t,k}$ stands for the additional generation term of turbulence kinetic energy induced by tubes. With the assumption that all the work done by the shell-side fluid is transformed into the turbulent kinetic energy at large speeds, the additional generation term can be expressed by the dot product of distributed resistance vector and velocity vector on the shell side [20,23], as shown in Eq. (13).

$$G_{t,k} = f_i \frac{1}{2}\rho u_i |u_i| \cdot u_i = \sum_i f_i \frac{1}{2}\rho |u_i|^3 \quad (13)$$

$G_{t,\varepsilon}$ represents the additional generation term of turbulent kinetic energy dissipation rate induced by tubes, which is calculated through Eq. (14).

$$G_{t,\varepsilon} = \frac{1.92\varepsilon}{k} G_{t,k} = \frac{1.92\varepsilon}{k} \sum_i f_i \frac{1}{2}\rho |u_i|^3 \quad (14)$$

2.2. Governing equation on the tube side

Since the fluid flows in the axial direction on the tube side and heat conduction is negligible, the flow and heat transfer of the tube side is simplified into a stable one-dimensional problem. In order that the tube-side conservation equation could be consistent with those of the shell side, Eq. (15) is presented as the energy conservation on the tube side.

$$\rho_t c_{p,t} u_t f_{S,t} \frac{dT_t}{dx} = -\beta K(T_t - T_s) \quad (15)$$

where u_t is the physical velocity of fluid on the tube side, while $f_{S,t}$ stands for the surface permeability of tube-side fluid.

3. Numerical computation and experimental validation

3.1. Geometry of the heat exchanger with flower baffles

Fig. 1 schematically illustrates the configuration of the heat exchanger with flower-baffles for the present simulation. The dimensions and other parameters, such as the Re numbers, are identical to those used in our previous experimental investigation [29]. It contains 24 tubes with an outer diameter of 16 mm, arranged in non-staggered form with a pitch of 20 mm. Eight pieces of flower baffles ($\alpha = 90°$) are installed alternately on the shell side with a spacing of 170 mm. The heat exchanger has double tube passes. Warm fresh water acts as the working fluid on the tube side, while cool fresh water is used for the shell side. The detailed structural parameters are listed in Table 1.

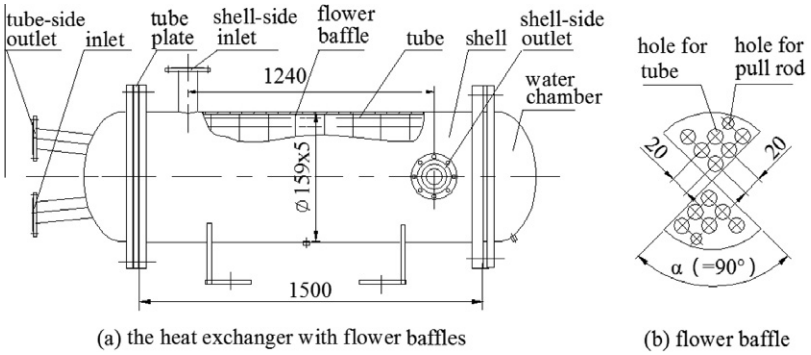

Fig. 1. Configuration of the heat exchanger with flower baffles (a), and sketch of the flower baffle (b).

Table 1
Structural parameters of the FB-STHX.

Tube material: stainless steel	Tube-side fluid: warm water
Tube-side pass number: 2	Tube arrangement: non-staggered
Tube number: 24	Tube effective length: 1473 mm
Tube pitch: 20 mm	Tube type: smooth
Tube inner diameter: 14.4 mm	Tube outer diameter: 16 mm
Shell inner diameter: 149 mm	Shell-side fluid: cool water
Baffle number: 8	Baffle arrangement: staggered
Baffle spacing: 170 mm	Baffle geometry angle: 90°
Shell-baffle gap: 2 mm	Baffle thickness: 4 mm
Pull rod number: 4	Pull rod diameter: 12 mm

3.2. Computation scheme

The whole volume involved in the shell, together with the inlet and outlet tubes, is taken as the computation domain, whose geometrical model is divided into two regions. One is the core region with tubes and the other includes the inlet and outlet tubes and the narrow region between the outermost tubes and the shell wall. The effects of leakages resulting from the gaps between the baffles and the shell wall are considered in the geometrical modeling and numerical computation. However, since the clearances between tubes and baffles are very small, their effects are expected to be negligible. Thus, we did not consider these leakage effects in the computation.

The popular CFD preprocessor, Gambit, is utilized for geometrical modeling and meshing. The geometrical model and grid system with hexahedral cells are shown in Fig. 2(a) and (b), respectively. The thickness of flower baffles is neglected.

Boundary conditions are set as follows: (1) No slip and no penetration are specified for all walls. (2) Zero heat flux is set upon the shell wall for the thermal boundary because the shell wall is thermally insulated in our experiment. (3) At the inlet of the shell side, a velocity profile of fully-developed turbulent flow is given, while the fluid temperature is set as uniform. (4) At the outlet of the shell side, a pressure-outlet condition is imposed.

In the core region where tubes are arranged, the volumetric porosity is set as the local volume ratio occupied by the shell-side fluid, while the impacts of tubes on the conservation equations of momentum, energy, turbulence kinetic energy and its dissipation rate are treated by introducing the corresponding source terms with six user defined functions (UDFs). As for the outer region without tubes, the volumetric porosity is set as unity and no source term is added.

Since the fluid temperature variation on the tube side was not so large in our experiment [29], the energy equation of tube side is not solved in the present computation. For simplicity, the lumped parameter, i.e., the averaged value of the inlet and outlet

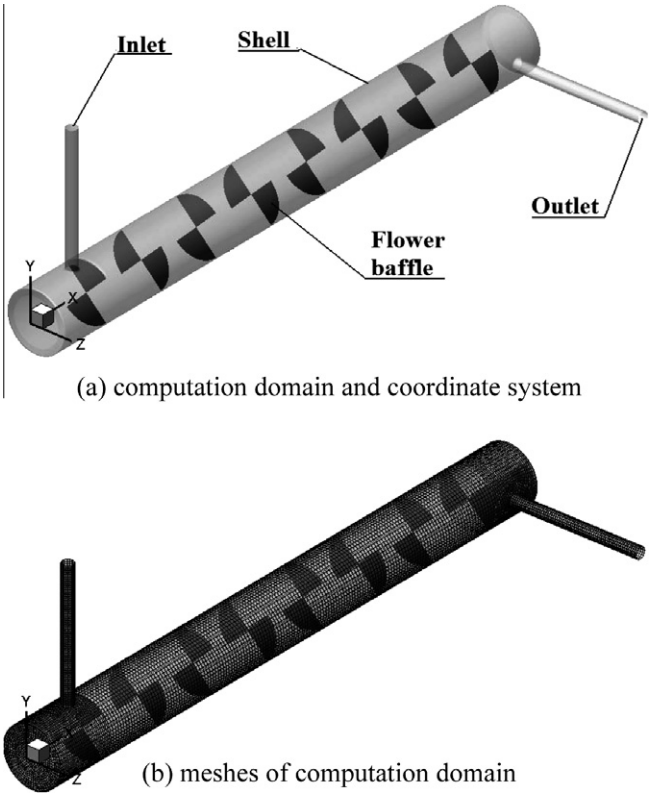

Fig. 2. Computation domain and coordinate system of the heat exchanger with flower baffles (a), and meshes of computation domain (b).

of the tube side, is adopted to calculate the local distributed heat source for the shell side. The shell-side fluid takes the formulation of apparent velocity, and the fluid physical properties depend on the temperature in the current computation.

The commercial CFD software, Fluent, is applied to undertake the task of numerical computation. The three-dimension, double-precision, pressure-based solver is adopted. The conservation equations accompanied by boundary conditions are discretized with finite volume formulation. The momentum and energy terms are treated with the second-order upwind scheme. The coupling between the pressure and velocity are realized through the 'SIMPLE' algorithm. The convergence criteria are set as: relative residual of 1E-8 for energy while 1E-5 for continuity and others. Three sets of grids (80,000, 150,000 and 320,000) are tried for the case of $Re = 7001$. It is found the relative difference between the mean convective heat transfer coefficient and total pressure drop of the latter two are less than 5%. Thus, the grid system of 150,000 is adopted for the final computation.

3.3. Data reduction

The mean heat transfer coefficient, K_m, is determined by Eq. (16).

$$K_m = \frac{Q}{A \cdot \Delta T_m} \tag{16}$$

where Q is the whole heat flux through tube walls which equals to the enthalpy difference between the inlet and outlet of the shell side, i.e., $Q = c_{p,s} m_s (T_{s,ex} - T_{s,in})$. A refers to the total heat transfer area based on the outer diameter of tubes, i.e., $A = n\pi d_o L$.

Eq. (17) is used for the computation of the mean temperature difference [29].

$$\Delta T_m = \frac{(T_{s,ex} - T_{s,in})\sqrt{R^2+1}}{\ln \frac{2-P(1+R-\sqrt{R^2+1})}{2-P(1+R+\sqrt{R^2+1})}} \tag{17}$$

where $R = \frac{T_{t,in} - T_{t,ex}}{T_{s,ex} - T_{s,in}}$, and $P = \frac{T_{s,ex} - T_{s,in}}{T_{t,in} - T_{s,in}}$.

With some operations performed on the Eq. (7), we obtain Eq. (18), through which the mean shell-side convective heat transfer coefficient could be calculated.

$$h_{s,m} = \frac{1}{\frac{1}{K_m} - \frac{d_o}{d_i}\frac{1}{h_{t,m}} - \frac{d_o}{2\lambda_w}\ln\frac{d_o}{d_i}} \tag{18}$$

where $h_{t,m}$ is the mean tube-side convective heat transfer coefficient, calculated with Eq. (8).

The shell-side characteristic dimension d_e and Reynolds number Re_s of the FB-STHX are defined through Eqs. (19) and (20), respectively.

$$d_e = \frac{D^2 - nd_o^2 - n_p d_p^2}{D + nd_o + n_p d_p} \tag{19}$$

$$Re_s = \frac{\rho u_e d_e}{\mu} \tag{20}$$

where n_p and d_p are respectively the number and diameter of pull rod, while u_e refers to the axial velocity at the breaches of flower baffles on the shell side.

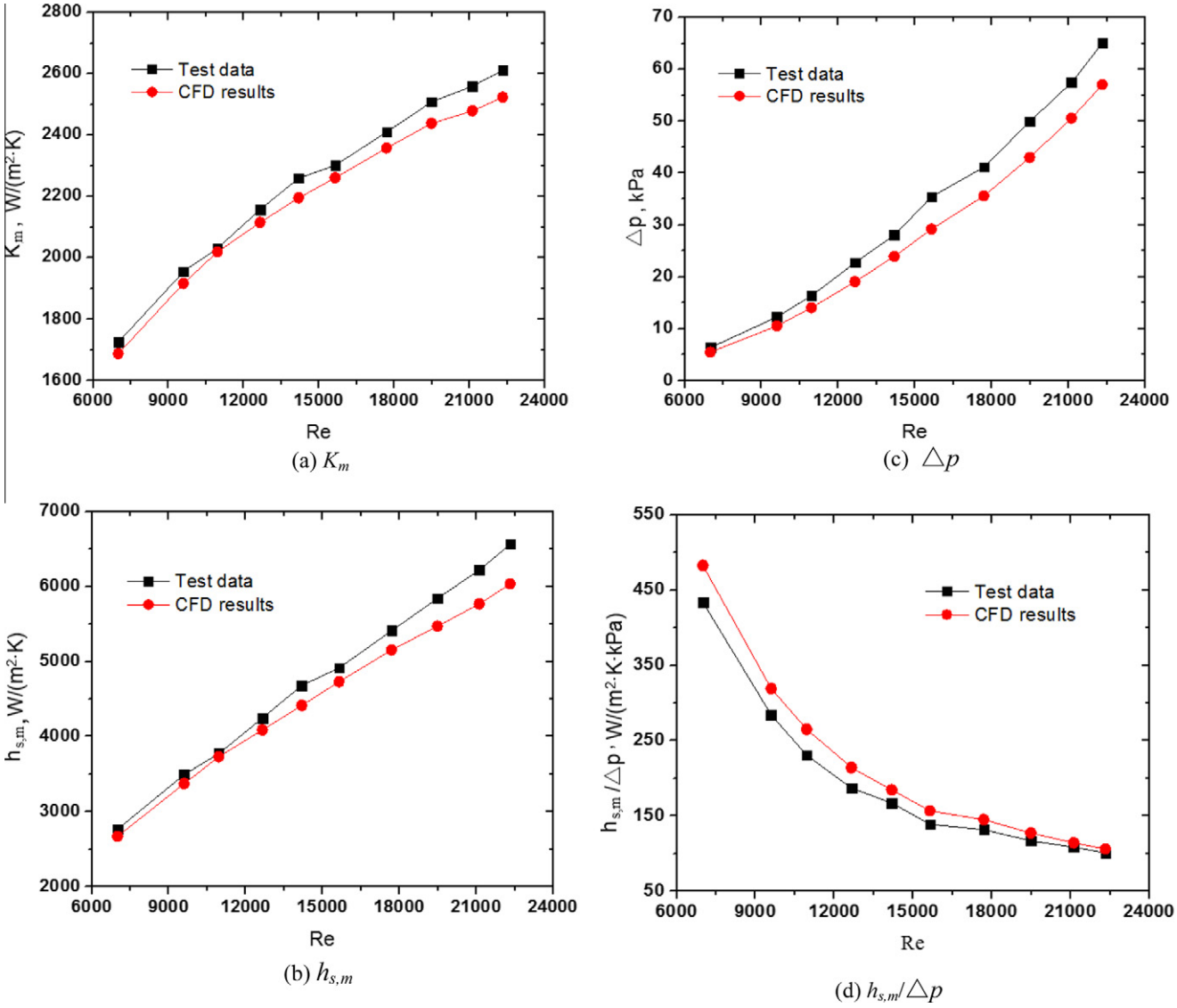

Fig. 3. Comparisons of the mean heat transfer coefficient K_m, mean convective heat transfer coefficient $h_{s,m}$ and total pressure loss Δp, as well as the overall performance index $h_{s,m}/\Delta p$ on the shell side between CFD results and test data for the heat exchanger with flower baffles, where tube-side fluid velocity is 1.2 m/s.

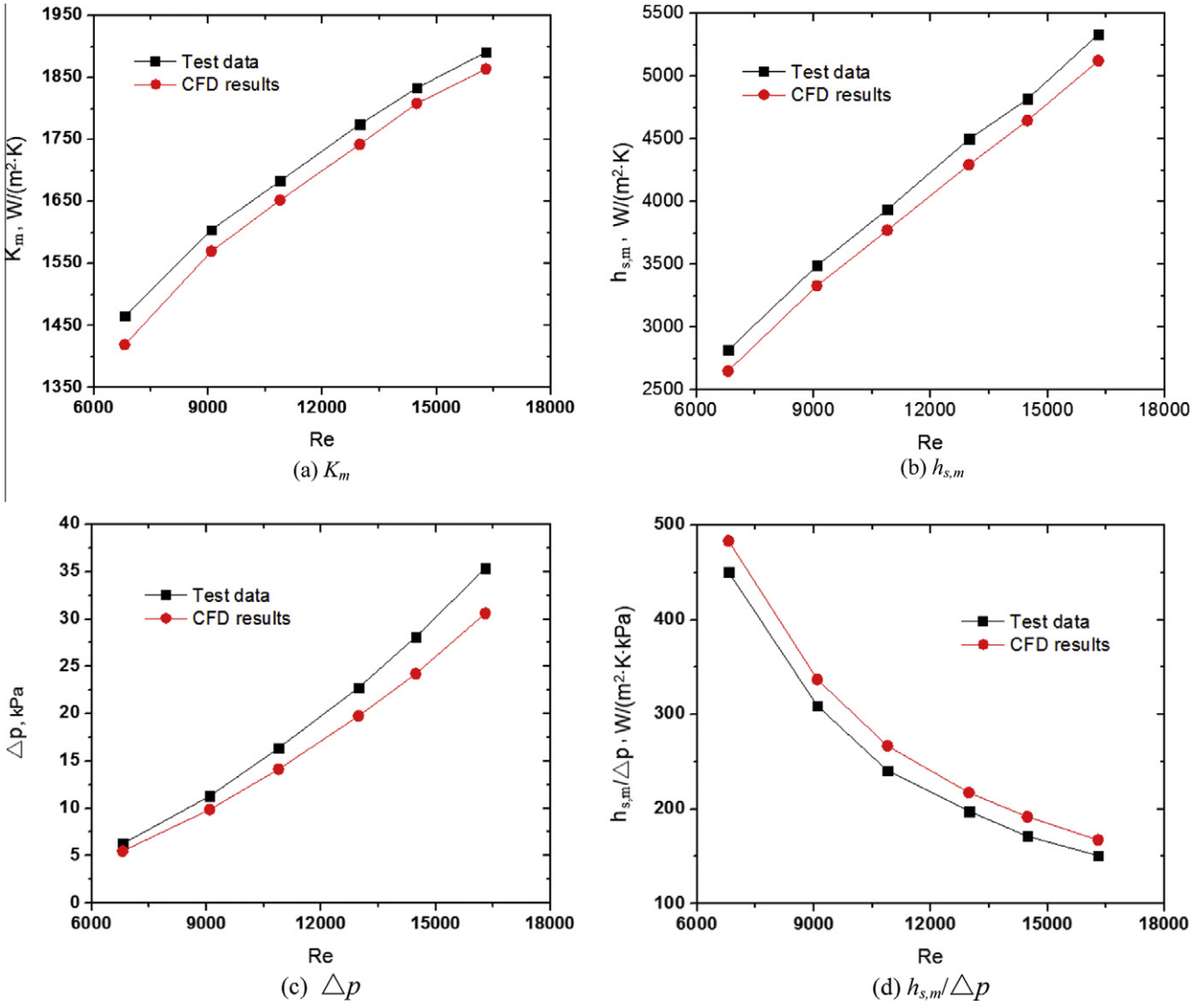

Fig. 4. Comparisons of the mean heat transfer coefficient K_m, mean convective heat transfer coefficient $h_{s,m}$ and total pressure loss Δp, as well as the overall performance index $h_{s,m}/\Delta p$ on the shell side between CFD results and test data for the heat exchanger with flower baffles, where tube-side fluid velocity is 0.7 m/s.

3.4. Computation results and experimental validation

In the current work, the computations were performed under the same conditions as the experiment [29], and comparisons of the lump parameters such as mean heat transfer coefficient and total pressure drop with those of experimental data were conducted for the validation of the simplified model. The calculated mean shell-side heat transfer coefficient $h_{s,m}$, total pressure drop Δp, and the ratio $h_{s,m}/\Delta p$ are presented in Figs. 3 and 4 for the cases with tube-side velocities of 1.2 and 0.7 m/s, respectively, in which the experimental data are also given for validation of the numerical model.

From Figs. 3 and 4 it is clearly seen that the mean heat transfer coefficient K_m, and convective heat transfer coefficient $h_{s,m}$ increase with the increase of the Reynolds number. The flow resistance Δp shows a similar variation tendency to those of K_m and $h_{s,m}$. However, the overall thermal hydraulic performance index, or the ratio $h_{s,m}/\Delta p$, exhibits a contrary behavior, i.e., it decreases with the increase of the Reynolds number. This is because the flow resistance Δp increases more rapidly than the mean convective heat transfer coefficient $h_{s,m}$. For more details, we take the case with a tube velocity of 1.2 m/s as an example. When the *Re* is raised from 7001 to 22,326, the mean convective heat transfer coefficient $h_{s,m}$ increases by about 2.5 times, while the pressure drop Δp increases by 6 times.

Comparing the numerical results with the experimental data, it is also noted that their variation tendencies are qualitatively consistent. To be more exactly, when the tube velocity is 1.2 m/s, the average relative deviations of K_m, $h_{s,m}$, Δp, and $h_{s,m}/\Delta p$ between the numerical results and test data are less than 3%, 8%, 14%, and 10%, respectively. In the case with a tube velocity of 0.7 m/s, the corresponding deviations of K_m, $h_{s,m}$, Δp, and $h_{s,m}/\Delta p$ are 3%, 6%, 14%, and 10%, respectively. These demonstrate that the numerical model has reasonable accuracy on the prediction of heat transfer rate and flow resistance.

To further confirm the present model, we conducted a computation of the heat exchanger with five segmental baffles of ~30% cut used at Argonne National Lab, whose shell diameter and length are respectively 0.59 and 3.58 m [30]. The calculated pressure profile was compared with those of experiment, as shown in Fig. 5. It

can be seen from Fig. 5 that the present numerical result agrees well with the experimental data.

4. Thermal augmentation analysis

From the numerical results and experimental data it is seen that the flower baffles can effectively enhance the heat transfer rate on the shell side. To help analyzing the underlying mechanism of the thermal augmentation, we take the case of $Re = 7001$ as an example to make a comparison between the heat exchangers without and with flower baffles. The velocity and temperature fields, together with the distributions of convective heat transfer coefficient on the shell side of the two heat exchangers, are presented in Figs. 6–11, respectively, in which the shell-side and tube-side flow rates of the heat exchanger without baffles are identical to those with baffles.

Fig. 6(a) and (b) depicts the contours of velocity magnitude in the longitudinal and horizontal sections of the heat exchanger without baffles. It is clearly seen from the figure that, for the case without baffles, the direction of the bulk flow is along the tubes axis in the central part on the shell side, and the velocity is relatively uniform. Therefore, the convective heat transfer coefficient on the shell side is relatively smaller, which can be seen from Fig. 7. As a result, the shell-side fluid is heated relatively slowly and the temperature at the outlet is low, as shown in Fig. 8.

The contours of velocity magnitude in the longitudinal and horizontal sections of the FB-STHX are presented in Fig. 9(a) and (b), respectively. Compared with the case of no baffles (see Fig. 6), it is seen that the velocity field of the FB-STHX becomes relatively complicated with the installation of flower baffles. To be more ex-

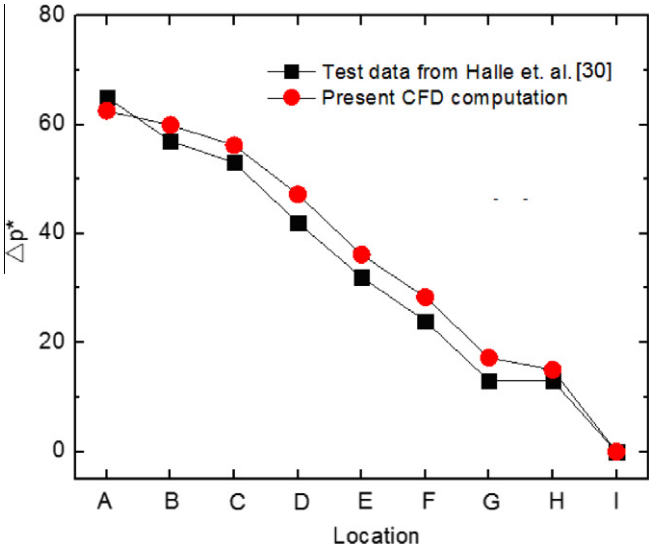

Fig. 5. Comparison of the non-dimensional pressure drops obtained by the present model with test data [30].

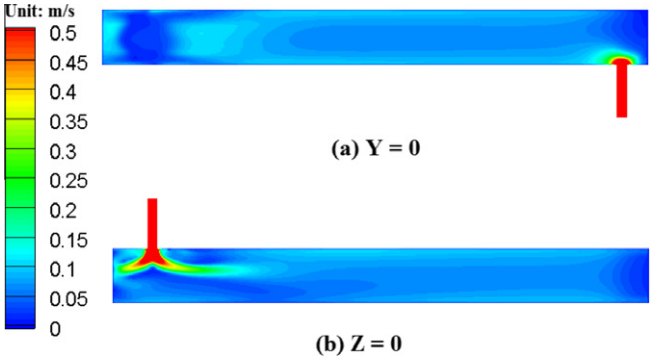

Fig. 6. Contours of shell-side velocity magnitude in the longitudinal and horizontal sections for the heat exchanger without baffles at the flow rate which is identical to that of FB-STHX at $Re = 7001$. (a) $Y = 0$ and (b) $Z = 0$.

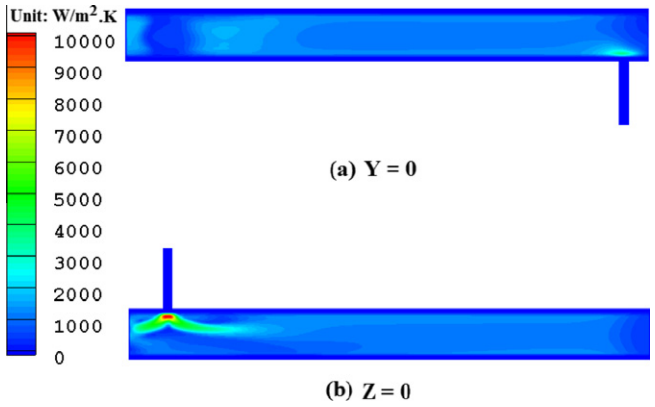

Fig. 7. Contours of shell-side convective heat transfer coefficient in the longitudinal and horizontal sections for the heat exchanger without baffles at the flow rate which is identical to that of FB-STHX at $Re = 7001$. (a) $Y = 0$ and (b) $Z = 0$.

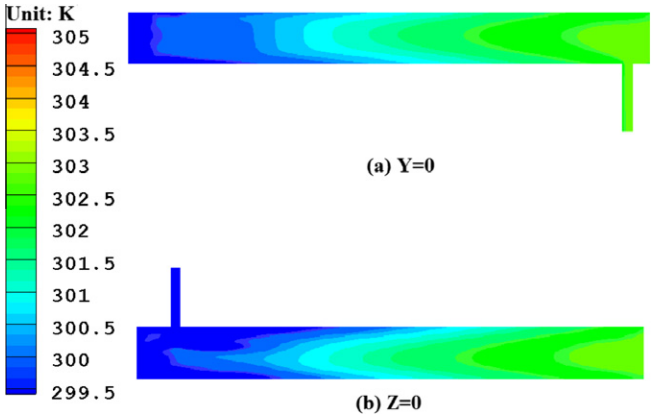

Fig. 8. Contours of shell-side fluid temperature in the longitudinal and horizontal sections for the heat exchanger without baffles at the flow rate which is identical to that of FB-STHX at $Re = 7001$. (a) $Y = 0$ and (b) $Z = 0$.

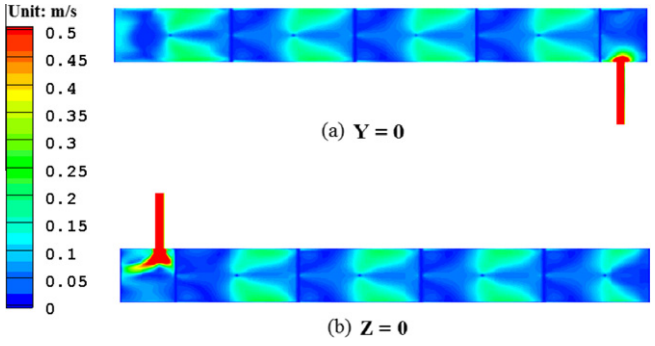

Fig. 9. Contours of shell-side velocity magnitude in the longitudinal and horizontal sections for the heat exchanger with flower baffles at $Re = 7001$. (a) $Y = 0$ and (b) $Z = 0$.

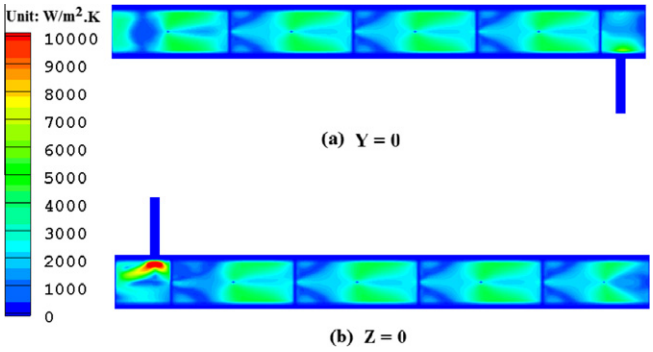

Fig. 10. Contours of shell-side convective heat transfer coefficient in the longitudinal and horizontal sections for the heat exchanger with flower baffles at Re = 7001. (a) Y = 0 and (b) Z = 0.

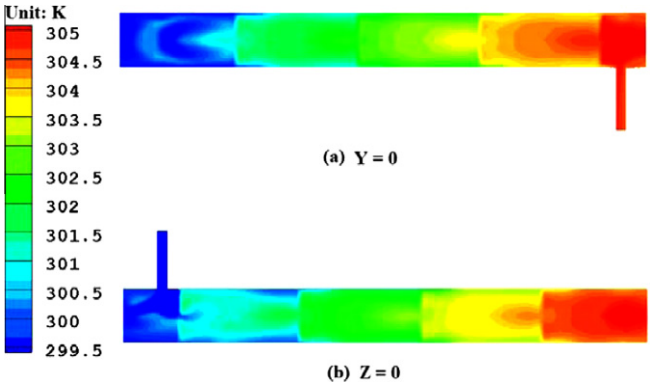

Fig. 11. Contours of shell-side fluid temperature in the longitudinal and horizontal sections for the heat exchanger with flower baffles at Re = 7001. (a) Y = 0 and (b) Z = 0.

actly, the fluid velocity magnitude on the shell side changes periodically in the central part of the FB-STHX. In more details, when the fluid passes a baffle, it is firstly accelerated rapidly and then flows across the breaches with large velocity. After rushing out of the breaches, the fluid is expanded suddenly and the velocity is decreased gradually. This periodic flow pattern is caused by the periodic changes of flow area which is induced by arrangement of flower baffles. Moreover, it is also seen in Fig. 9 that in the downstream just behind a baffle, two recirculation flow regions are generated, where the velocity magnitude is very small.

Fig. 10 presents the distribution of the local convective heat transfer coefficient on the shell side for the FB-STHX. Compared with the contours of velocity field (see Fig. 9), the convective heat transfer coefficient also changes periodically in the central part of the FB-STHX, and its pattern is similar to that of flow field. To be more exactly, it can be seen from Figs. 9 and 10 that where the fluid velocity magnitude is higher, the heat transfer rate is larger. In more details, in the downstream of the breaches, where the fluid washes the tubes with large velocity, the convective heat transfer coefficient is also large. While in the downstream just behind the baffle, where two recirculation flow regions with low velocity are generated, the convective heat transfer coefficient is small as well. At other places, both the velocity magnitude and convective heat transfer coefficient are moderate. The mean heat transfer rate of the shell side depends on the compromise of the above three aspects. As for the investigated cases, the region with large convective heat transfer coefficient is broad, while the impact of the recirculation flow regions is limited. Therefore, the mean

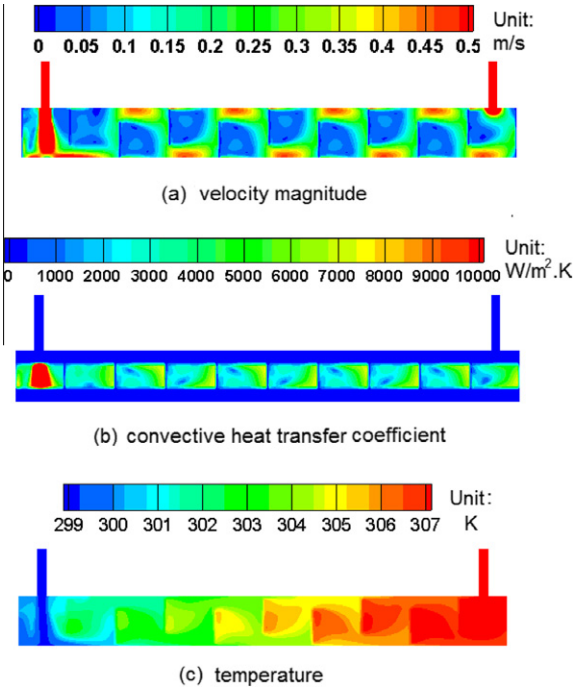

Fig. 12. Contours of shell-side fluid velocity magnitude, convective heat transfer coefficient and temperature in the symmetrical section for the heat exchanger with segmental baffles at the flow rate which is identical to that of FB-STHX at Re = 7001.

shell-side heat transfer rate is effectively enhanced by the flower baffles.

The variation of fluid temperature depends strongly on the convective heat transfer coefficient. In other words, the larger the convective heat transfer coefficient, the larger variation the fluid temperature has. Fig. 11(a) and (b) depicts the fluid temperature fields in the longitudinal and horizontal sections of the FB-STHX. Compared with the case of no baffle (see Fig. 8), It is clearly observed that the fluid temperature of FB-STHX changes far more quickly along the flow direction, and the outlet temperature is much higher under the same inlet condition, which confirms that the mean convective heat transfer rate on the shell side is effectively enhanced by the flower baffles.

The shell-and-tube heat exchanger with nine segmental baffles of ~16% cut [29], was also computed with the above-mentioned method at about the same shell- and tube-side flow rate as the FB-STHX. Dimensions of the shell and tubes of the SG-STHX are identical to those of the FB-STHX. The calculated shell-side fluid velocity, convective heat transfer coefficient and fluid temperature of the SG-STHX are depicted in Fig. 12(a)–(c), respectively. Similar to those of FB-STHX, the velocity magnitude and local convective heat transfer coefficient vary periodically on the central part of the shell side. Comparing the contours of velocity magnitude between FB-STHX and SG-STHX (see Figs. 9 and 12(a)), it can be seen that they have different flow patterns, i.e., the shell-side fluid of SG-STHX flows in the Zigzag mode, while spiral flow is generated in the FB-STHX. Moreover, in the SG-STHX, the fluid has relatively larger velocity and recirculation region between two baffles is also larger. Affected by the shell-side flow pattern, the shell-side convective heat transfer coefficient and fluid temperature of the SG-STHX are higher than the counterparts of FB-STHX, as shown in Figs. 10–12(b)–(c). Meanwhile, the flow resistance of SG-STHX is larger than that of FB-STHX. Consequently, the overall shell-side performance index, $h_{s,m}/\Delta p$, of the FB-STHX (483 W/(m^2 K kPa)) is larger than that of SG-STHX (395 W/(m^2 K kPa)). This demonstrates that the FB-STHX has a better thermal hydraulic performance than the SG-STHX, which is also consistent with the experimental results [29].

5. Conclusions

In the present study, a numerical model based on the concepts of porosity and permeability was developed for the shell-side flow and heat transfer of shell-and-tube heat exchangers (STHXs), in which the distributed resistance and heat source, as well as the distributed turbulence kinetic energy and its dissipation rate were introduced to account for the impacts of tubes on fluid. The numerical model is solved at shell-side Reynolds numbers ranging from 6813 to 22,326 for a STHX with flower baffles, and reasonable accuracy is demonstrated by the comparison with test data. The contours of the velocity and temperature fields, together with the distribution of convective heat transfer coefficient on the shell side, were obtained for the heat exchangers with and without flower baffles. The underlying mechanism of shell-side thermal augmentation was analyzed based on the comparisons between these distributions of the two heat exchangers. It is clearly seen that with the installation of flower baffles, the fluid velocity magnitude and convective heat transfer coefficient vary in a periodical way in the central part of the FB-STHX, and three regions with small, moderate or large convective heat transfer coefficients are generated after the flower baffles. The overall heat transfer enhancement on the shell side depends on their compromise. As for the investigated FB-STHX, the heat transfer rate is effectively enhanced on the shell side. Moreover, a comparison of contours between FB-STHX and SG-STHX was performed. It is found that they have different flow patterns, and the FB-STHX has a better overall thermal hydraulic performance than the SG-STHX.

In summary, the present numerical model is a powerful tool to predict the thermal hydraulic performances of the shell-and-tube heat exchanger with relatively low computation cost. Moreover, it can also provide details of the flow and temperature fields which help to analyze the underlying mechanism of thermal augmentation.

Acknowledgments

This work was financially supported by the Projects of Natural Science Foundations of China (Nos. 51036003, 51076054 and 51076057).

References

[1] A.E. Bergles, ExHFT for fourth generation heat transfer technology, Exp. Therm. Fluid Sci. 26 (2–4) (2002) 335–344.
[2] A.W. Fan, J.J. Deng, J. Guo, W. Liu, A numerical study on thermo-hydraulic characteristics of turbulent flow in a circular tube fitted with conical strip inserts, Appl. Therm. Eng. 31 (2011) 2819–2828.
[3] A.W. Fan, J.J. Deng, A. Nakayama, W. Liu, Parametric study on turbulent heat transfer and flow characteristics in a circular tube fitted with louvered strip inserts, Int. J. Heat Mass Transfer 55 (2012) 5205–5213.
[4] Y.H. You, A.W. Fan, W. Liu, S.Y. Huang, Thermo-hydraulic characteristics of laminar flow in an enhanced tube with conical strip inserts, Int. J. Therm. Sci. (2012), http://dx.doi.org/10.1016/j.ijthermalsci.2012.06.013.
[5] J. Yang, M. Zeng, Q. Wang, A. Nakayama, Forced convection heat transfer enhancement by porous pin fins in rectangular channels, J. Heat Transfer – Trans. ASME 132 (2010). 051702-1-8.
[6] R. Mukherjee, Use double-segmental baffles in the shell-and-tube heat exchangers, Chem. Eng. Prog. 88 (1992) 47–52.
[7] R. Mukherjee, Effectively design shell-and-tube heat exchanger, Chem. Eng. Prog. 94 (2) (1998) 21–37.
[8] H. Li, V. Kottke, Effect of baffle spacing on pressure drop and local heat transfer in shell-and-tube heat exchangers for staggered tube arrangement, Int. J. Heat Mass Transfer 41 (10) (1998) 1303–1311.
[9] W.M. Song, J.A. Meng, Z.X. Li, Optimization of flue gas turbulent heat transfer with condensation in a tube, Chin. Sci. Bull. 56 (19) (2011) 1978–1984.
[10] E. Ozden, I. Tari, Shell side CFD analysis of a small shell-and-tube heat exchanger, Energy Convers. Manage. 51 (2010) 1004–1014.
[11] V.V. Wadekar, P. Sthlik, Different strategies to improve industrial heat exchanger, Heat Transfer Eng. 23 (6) (2002) 36–48.
[12] S.J. Green, G. Hetsroni, PWR steam generators, Int. J. Multiph. Flow 21 (1995) 1–97.
[13] C.C. Gentry, Rodbaffle heat exchanger technology, Chem. Eng. Prog. 86 (7) (1990) 48–57.
[14] W. Liu, Z.C. Liu, Y.S. Wang, S.Y. Huang, Flow mechanism and heat transfer enhancement in longitudinal-flow tube bundle of shell-and-tube heat exchanger, Sci. China Ser. E-Tech. Sci. 52 (10) (2009) 2952–2959.
[15] D. Kral, P. Stelik, H.J. Van der Ploeg, B.I. Master, Helical baffles in shell-and-tube heat exchangers, part I: experimental verification, Heat Transfer Eng. 17 (1) (1996) 93–101.
[16] J. Lutcha, J. Nemcansky, Performance improvement of tubular heat exchangers by helical baffles, Chem. Eng. Res. Des. 68 (3) (1990) 263–270.
[17] X. Deng, S. Deng, Investigation of heat transfer enhancement of roughened tube bundles supported by ring or rod supports, Heat Transfer Eng. 19 (2) (1998) 21–27.
[18] S.V. Patankar, D.B. Spalding, A calculation for the transient and steady-state behavior of shell-and-tube heat exchangers, in: A.A. Afgan, E.U. Schluner (Eds.), Heat Transfer Design and Theory Sourcebook, Hemisphere Publishing Corporation, Washington, 1974, pp. 155–176.
[19] D.B. Rhodes, L.N. Carlucci, Predicted and measured velocity distributions in a model heat exchanger, in: Int. Conf. on Numerical Methods in Engineering, Canadian Nuclear Society/American Nuclear Society, 1983, pp. 935–948.
[20] M. Prithiviraj, M.J. Andrews, Three dimensional numerical simulation of shell-and-tube heat exchanger. Part I: foundation and fluid mechanics, Numer. Heat Transfer, Part A 33 (1998) 799–816.
[21] M. Prithiviraj, M.J. Andrews, Three-dimensional numerical simulation of shell-and-tube heat exchangers, Part II: heat transfer, Numerical Heat Transfer, Part A 33 (1998) 817–828.
[22] Z. Stevanovic, G. Ilic, N. Radojkovic, M. Vukic, V. Stefanovic, G. Vuckovic, Design of shell-and-tube heat exchanger by using CFD technique – Part one: thermo-hydraulic calculation, Mech. Eng. 1 (8) (2001) 1091–1105.
[23] Y.L. He, W.Q. Tao, B. Deng, X. Li, Y. Wu, Numerical simulation and experimental study of flow and heat transfer characteristics of shell side fluid in shell-and-tube heat exchangers, in: R.K. Shah, M. Ishizuka, T.M. Rudy, V.V. Wadekar (Eds.), Proc. Fifth Int. Conf. on Enhanced, Compact and Ultra-Compact Heat Exchangers: Science, Engineering and Technology, Engineering Conferences International, Hoboken, NJ, USA, 2005, pp.29–42.
[24] X. Huang, Z. Lu, Q. Wang, Numerical modeling of the shell side flow in shell-and-tube heat exchangers, in: W. Liu (Ed.), Proc. Int. Conf. on Energy Conversion and Application, vol. 1, Wuhan, China, 2001, pp. 301–304.
[25] Y. Li, X. Jiang, X. Huang, J. Jia, J. Tong, Optimization of high-pressure shell-and-tube heat exchanger for syngas cooling in an IGCC, Int. J. Heat Mass Transfer 53 (2010) 4543–4551.
[26] Q.W. Wang, G.N. Xie, M. Zeng, L.Q. Luo, Prediction of heat transfer rates for shell-and-tube heat exchangers by artificial neutral networks approach, J. Therm. Sci. 15 (2006) 257–262.
[27] B. Peng, Q.W. Wang, C. Zhang, G.N. Xie, L.Q. Luo, Q.Y. Chen, M. Zeng, An experimental study of shell-and-tube heat exchangers with continuous helical baffles, J. Heat Transfer – Trans. ASME 129 (2007) 1425–1431.
[28] Y.G. Lei, Y.L. He, L. Rui, Y.F. Gao, Effects of baffle inclination angle on flow and heat transfer of a heat exchanger with helical baffles, Chem. Eng. Process. 47 (2008) 2336–2345.
[29] Y. Wang, Z. Liu, S. Huang, W. Liu, W. Li, Experimental investigation of shell-and-tube heat exchanger with a new type of baffles, Heat Mass Transfer 47 (2011) 833–839.
[30] H. Halle, J.M. Chenoweth, M.W. Wambsganss, Shell side water flow pressure drop distribution measurements in an industrial-sized test heat exchanger, in: A Reappraisal of Shell Side Flow in Heat Exchangers, 22nd Heat Transfer Conference and Exhibition, ASME, Niagara Falls, 1984, pp. 37–48.
[31] "Steam generator" editorial group, Steam generator, Atomic Energy Press (in Chinese), Beijing, 1982, pp. 130–135.
[32] J.P. Holman, Heat Transfer, McGraw-Hill, New York, 1997. pp. 274–275.
[33] A. Zukauskas, Heat transfer from tubes in cross flow, in: J.P. Hartnett, T.F. Irvine Jr (Eds.), Advances in Heat Transfer, vol. 8, Academic Press, New York, 1972, pp. 93–158.